JOURNAL OF PROPULSION AND POWER
Vol. 11, No. 4, July–August 1995

Effects of Acoustic Oscillations on Flame Dynamics of Homogeneous Propellants in Rocket Motors

Tae-Seong Roh,* I-Shih Tseng,† and Vigor Yang‡
Pennsylvania State University, University Park, Pennsylvania 16802

The interactions between acoustic waves and gas-phase flame dynamics of a double-base homogeneous propellant in a rocket motor has been studied by means of a comprehensive numerical analysis. The formulation treats the complete conservation equations of mass, momentum, energy, and species concentration, and accounts for finite rate chemical kinetics in the gas phase and subsurface reactions. The model has been implemented to examine the detailed flow structures and heat-release mechanisms in various parts of the motor, including microscale motions near the propellant surface and macroscale motions in the bulk of the chamber. Results indicate that strong interactions between exothermic reactions and acoustic waves occur in regions with steep temperature gradients due to the large activation energy of the associated chemical kinetics. The dynamic behavior of the luminous flame plays a decisive role in determining the motor stability characteristics. Distributed combustion response in the gas phase provides the energy for driving flow oscillations, and can be treated correctly as a combination of monopole and dipole sources based on acoustic theory.

Nomenclature

A = pre-exponential factor for gas-phase reaction
B = pre-exponential factor for condensed-phase reaction
C_c = specific heat of condensed phase
C_p = specific heat of gas
E_i = activation energy
$\boldsymbol{E}, \boldsymbol{F}$ = convective flux vectors
$\boldsymbol{E}_v, \boldsymbol{F}_v$ = diffusion flux vectors
e = specific total internal energy
H = chamber half-height
$h^0_{f,i}$ = heat of formation of species i
h_i = specific enthalpy of species i
L = chamber length
$\dot{m}$ = mass flow rate
N = number of species considered in gas phase reactions
p = pressure
Q_c = total heat release in condensed phase
Q_i = heat release from reaction of species i
$\boldsymbol{Q}$ = dependent variable vector
$\dot{q}_c$ = rate of heat release in condensed phase per unit volume
q_e = thermal diffusion term
q_i = mass diffusion term
R_u = universal gas constant
r_b = propellant burning rate
$\boldsymbol{r}$ = spatial coordinates
$\boldsymbol{S}$ = source vector
T = temperature or period of oscillation
T_i = initial conditioned temperature of propellant
T_s = temperature at propellant surface
t = time
u, v = bulk velocities in axial and vertical directions, respectively
$\hat{u}_i, \hat{v}_i$ = diffusion velocities of gas-phase species i in axial and vertical directions, respectively
V = volume
$\bar{W}$ = molecular weight of mixture
W_i = molecular weight of species i
x, y = Cartesian coordinates
Y_i = mass fraction of species i
λ = thermal conductivity
ρ = density
τ = viscous stress
$\dot{\omega}_i$ = rate of production of species i

Subscripts
c = condensed phase
g = gas phase
i = ith species or initial condition
p = propellant
s = burning surface

Superscripts
T = transpose of vector
$'$ = fluctuating quantity

I. Introduction

THE phenomenon of combustion instability in a solid-propellant rocket motor results from interactions between acoustic waves and unsteady combustion processes in a confined volume. Acoustic flow oscillations cause local changes in mixing and combustion processes in the gas phase. Subsequent variation of heat transfer to the condensed phase alters the surface pyrolysis and burning characteristics of the propellant. This in turn produces acoustic disturbances by virtue of unsteady mass, momentum, and energy additions to the gas stream. When the process occurs at proper spatial locations and temporal phases with respect to acoustic motions, an energy feedback loop may be established and substantial pressure oscillations are excited and sustained.

Early work focused on the transient combustion responses of propellants to incident pressure oscillations, with only the one-dimensional mass and energy transport normal to the propellant surface taken into account.[1,2] The resultant pressure-coupled response function was treated as a propellant property and used to characterize the stability behavior of a rocket motor.[3] In spite of their contributions to the knowledge

Received May 25, 1995; revision received June 2, 1995; accepted for publication June 6, 1995.

*Graduate Research Assistant, Department of Mechanical Engineering.

†Professor, Department of Mechanical Engineering. Associate Fellow AIAA.

base of combustion instability, existing models provide limited information concerning propellant burning behavior in oscillatory crossflows under conditions representative of realistic motor environments. The major obstacle arises from the difficulties in treating various complicated physicochemical processes involved in unsteady combustion of propellants. Specifically, the following issues need to be resolved in order to achieve a thorough understanding of the key mechanisms responsible for driving instabilities in rocket motors: 1) how unsteady motor internal flow is established by propellant combustion, 2) how local flow disturbances affect propellant burning characteristics, and 3) what sort of interactions exist between chamber dynamics and transient combustion responses of propellants.

As a first attempt to address these fundamental issues, the present work concentrates on the effect of acoustic oscillations on flame dynamics in the gas phase. Emphasis is placed on energy-release processes and their iterations with local flow oscillations that drive motor instabilities. The transient responses of propellant combustion to acoustic motions will be treated in a parallel effort.[4] The primary purpose is to conduct a unified investigation into the ways in which oscillatory gas-phase heat release couples to and influences the evolution of unsteady motions in a rocket motor. Detailed flow characteristics are studied systematically, including microscale processes near the propellant surface where dominant exothermic reactions occur and macroscale processes associated with the unsteady gasdynamics in the bulk of the chamber.

In subsequent sections, a theoretical formulation of homogeneous propellant combustion in a rocket motor is first established, followed by a brief description of the numerical algorithm used in this work. The analysis starts with calculation of the motor internal flowfields under steady operating conditions, with propellant burning rates predicted as part of the solution. Periodic pressure oscillations are then imposed at the exit to simulate standing acoustic waves in the chamber. Various distinct features of unsteady motions and their influence on flame dynamics are investigated in depth. Special attention is given to the multidimensionality of flow disturbances and the response of heat-release processes in various regimes of reaction zones.

II. Theoretical Formulation

Figure 1 shows the situation examined here, a two-dimensional rocket motor loaded with a double-base homogeneous propellant grain. The formulation follows the model established in Ref. 5, but with an improved reaction mechanism a more detailed investigation into the interactions between acoustic oscillations and flame dynamics can be conducted. The analysis of the gas-phase process is based on the complete conservation equations of mass, momentum, energy, and species concentration, and takes into account finite-rate chemical kinetics and variations of thermophysical properties with temperature. The flow is assumed to be laminar in order to concentrate on the effect of flow disturbances on unsteady heat-release mechanisms without complications arising from turbulent transport. In vector notation, the set of conservation equations for a multicomponent chemically reacting system of N species can be written as

$$\frac{\partial \boldsymbol{Q}}{\partial t} + \frac{\partial}{\partial x}(\boldsymbol{E} - \boldsymbol{E}_v) + \frac{\partial}{\partial y}(\boldsymbol{F} - \boldsymbol{F}_v) = \boldsymbol{S} \tag{1}$$

where x and y represent the axial and vertical coordinates, respectively. The conserved variable vector $\boldsymbol{Q}$, convective flux vectors $\boldsymbol{E}$, $\boldsymbol{F}$, and diffusion-flux vectors $\boldsymbol{E}_v$, $\boldsymbol{F}_v$ are defined next:

$$\boldsymbol{Q} = [\rho, \rho u, \rho v, \rho e, \rho Y_i]^T \tag{2}$$

$$\boldsymbol{E} = [\rho u, \rho u^2 + p, \rho uv, (\rho e + p)u, \rho u Y_i]^T \tag{3}$$

$$\boldsymbol{F} = [\rho v, \rho uv, \rho v^2 + p, (\rho e + p)v, \rho v Y_i]^T \tag{4}$$

$$\boldsymbol{E}_v = [0, \tau_{xx}, \tau_{xy}, u\tau_{xx} + v\tau_{xy} - q_{e_x}, -q_{i_x}]^T \tag{5}$$

$$\boldsymbol{F}_v = [0, \tau_{xy}, \tau_{yy}, u\tau_{xy} + v\tau_{yy} - q_{e_y}, -q_{i_y}]^T \tag{6}$$

$$\boldsymbol{S} = [0, 0, 0, 0, \dot{\omega}_i]^T \tag{7}$$

where subscript i stands for species i, ranging from 1 to $N - 1$. In these equations, ρ, u, v, Y_i, and τ represent the density, axial and vertical velocity components, mass fraction of species i, and viscous stress, respectively. The thermal diffusion terms q_{e_x} and q_{e_y} consist of contributions from heat conduction and mass diffusion processes. Fick's law is used to approximate species diffusion terms q_{i_x} and q_{i_y}. For a multicomponent mixture, pressure and temperature can be calculated iteratively from the following thermodynamic relation and equation of state:

$$e = \sum_{i=1}^{N} Y_i h_i - \frac{p}{\rho} + \frac{1}{2}(u^2 + v^2)$$
$$h_i = h_{fi}^0 + \int_{T_{\text{ref}}}^{T} C_{pi}\, dT \tag{8}$$

$$p = \rho R_u T \sum_{i=1}^{N} \frac{Y_i}{W_i} \tag{9}$$

where h_i and W_i are the specific enthalpy and molecular weight of species i, respectively.

Within the pressure and temperature ranges of practical rocket-motor environments, thermal conductivity and viscosity of each species are basically functions of temperature only. They can be well approximated by fourth-order polynomials of temperature, with the coefficients of these polynomials supplied by McBride et al.[6] and valid for a temperature range from 300 to 6000 K. For mixtures, the specific heat is obtained by mass-concentration weighting of each species. Thermal conductivity and viscosity are calculated using Wilke's mixing rule.[7]

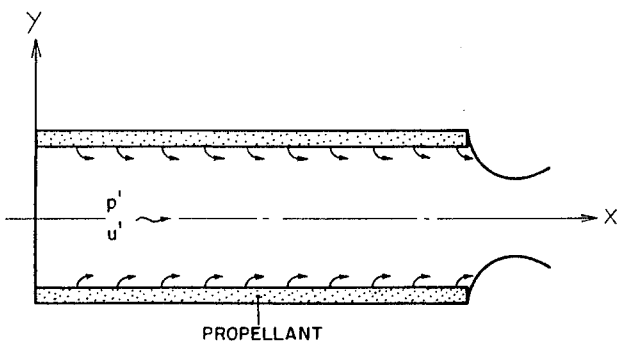

Fig. 1 Schematic diagram of a solid rocket motor.

A. Chemical Kinetics Model

Owing to the difficulties in establishing a complete chemical kinetics scheme and limitations of computational resources, a thorough consideration of all physical and chemical processes does not appear feasible. A reduced reaction mechanism is therefore used to describe the combustion-wave structure in both the gas and condensed phases. This model is a viable alternative that provides well-resolved and reasonably accurate information about major chemical kinetic pathways.

The scheme is developed following a careful review of existing models[8-13] and experimental data[13-15] for double-base propellant combustion. In brief, two global reactions in the condensed phase are proposed, including molecular degradation initiated by the rupture of O-NO_2 bond and ensuing reactions of NO_2 and aldehydes. These two reactions provide the elementary species [i.e., NO_2, NO, CH_2O, $(CHO)_2$, etc.], essential for maintaining the gas-phase flame:

$$\text{double-base propellant} \rightarrow 2.49NO_2 + 2.36CH_2O + 1.26(CHO)_2 + 0.17CO + \text{minor residuals} \quad \text{(R1)}$$

$$NO_2 + 0.56CH_2O + 0.16(CHO)_2 \rightarrow NO + 0.38\,CO + 0.5CO_2 + 0.5H_2O + 0.22H_2 \quad \text{(R2)}$$

The stoichiometric coefficients in reaction (R1) are determined based on the composition of a "hot" double-base propellant containing 52% nitrocellulose (NC), 43% nitroglycerin (NG), and 5% minor additives.[13] The heat of combustion of the propellant is about 1100 cal/g, similar to that of EC-1 propellant studied by Aoki and Kubota.[15] The coefficients in reaction (R2) represent a revision of those suggested by Faddoul et al.[12] in order to match experimental results of species concentrations and temperature at the surface. The rates of production of the nondegraded propellant and NO_2 are given next:

$$\dot{\omega}_c = -B_c \exp[(-E_c)/R_uT]\rho_c \quad (10)$$

$$\dot{\omega}_{NO_2} = Y_{NO_2{}_0}\dot{\omega}_c - B_{NO_2}p^{0.39} \exp[(-E_{NO_2})/R_uT]\rho_g Y_{NO_2} \quad (11)$$

where subscripts c and g stand for the condensed and gas phases, respectively, and R_u is the universal gas constant. The pressure dependence in Eq. (11) is required for a better prediction of burning characteristics (i.e., regression rate, surface temperature, and condensed-phase heat release) under various operating conditions, especially in the high-pressure range.

Following the suggestions of Lengelle et al.[10,13] and Bizot and Beckstead,[11] gas-phase kinetics are grouped into five global reactions: two first-order NO_2 and NO-carbon reactions, and three second-order reactions involving aldehydes and NO. These reactions represent the most important and slowest steps limiting the reaction rates in the gas phase, even though many other intermediate reactions take place:

$$NO_2 + 0.56CH_2O + 0.16(CHO)_2 \rightarrow NO + 0.38CO + 0.5CO_2 + 0.5H_2O + 0.22H_2 \quad \text{(R3)}$$

$$CH_2O + CH_2O \rightarrow CO + 0.5C_2H_4 + H_2O \quad \text{(R4)}$$

$$(CHO)_2 + (CHO)_2 \rightarrow 4CO + 2H_2 \quad \text{(R5)}$$

$$NO + 0.16CO + 0.12C_2H_4 + 0.12H_2 \rightarrow 0.5N_2 + 0.40CO_2 + 0.36H_2O \quad \text{(R6)}$$

$$C + NO \rightarrow CO + 0.5N_2 \quad \text{(R7)}$$

Note that most of the NO_2 and aldehyde reactions that form NO, CO, CO_2, and H_2O occur in the primary flame zone due to their relatively low activation energies. The highly exothermic reduction of NO to N_2, (R6), usually proceeds in the secondary flame zone and provides the major heat source for raising the flame temperature to its final value. The reaction of carbon and NO, (R7), is included to obtain the correct dark-zone temperature and thickness.[8] Although the mass fraction of solid carbon at the propellant surface is quite small (ranging from about 2.5% at 10 atm to 2.0% at 100 atm), this reaction releases an appreciable amount of energy owing to its large heat of combustion, and consequently plays an important role in determining the dark-zone behavior. The rate of production of each constituent species can be written in the following form:

$$\dot{\omega}_{NO_2} = -A_{NO_2}p^{0.39} \exp\left(\frac{-E_{NO_2}}{R_uT}\right)\rho_g Y_{NO_2} \quad (12)$$

$$\dot{\omega}_{CH_2O} = -0.56\frac{W_{CH_2O}}{W_{NO_2}}\dot{\omega}_{NO_2} - A_{CH_2O} \exp\left(\frac{-E_{CH_2O}}{R_uT}\right)\rho_g^2 Y_{CH_2O}^2 \quad (13)$$

$$\dot{\omega}_{(CHO)_2} = -0.16\frac{W_{(CHO)_2}}{W_{NO_2}}\dot{\omega}_{NO_2} - A_{(CHO)_2} \exp\left[\frac{-E_{(CHO)_2}}{R_uT}\right]\rho_g^2 Y_{(CHO)_2}^2 \quad (14)$$

$$\dot{\omega}_{NO} = \frac{W_{NO}}{W_{NO_2}}\dot{\omega}_{NO_2} - \frac{W_{NO}}{W_{carb}}\dot{\omega}_{carb} - A_{NO} \exp\left(\frac{-E_{NO}}{R_uT}\right)\rho_g^2 Y_{NO}^2 \quad (15)$$

$$\dot{\omega}_{carb} = -A_{carb}p\bar{W} \exp\left(\frac{-E_{carb}}{R_uT}\right)\rho_g Y_{carb}Y_{NO} \quad (16)$$

where the pressure term in Eqs. (12) and (16) has the unit of atm, and $\bar{W}$ represents the mean molecular weight of the gas mixture.

B. Condensed-Phase Process

The condensed phase consists of a preheated zone and a superficial degradation layer in which thermal decomposition of the propellant and the reaction of the decomposed species take place simultaneously. If we ignore the bulk motion, mass diffusion, and axial thermal diffusion, with the assumption of constant thermophysical properties, the formulation governing condensed-phase processes reduces to the following set of one-dimensional equations:

Mass

$$\dot{m} = \rho_c r_b \quad (17)$$

Energy

$$\rho_c C_c \frac{\partial T}{\partial t} + \dot{m}C_c \frac{\partial T}{\partial y} = \lambda_c \frac{\partial^2 T}{\partial y^2} + \dot{q}_c \quad (18)$$

Species concentration

$$\rho_c \frac{\partial Y_i}{\partial t} + \dot{m}\frac{\partial Y_i}{\partial y} = \dot{\omega}_i \quad (19)$$

where ρ_c denotes propellant density and r_b burning rate. The rate of condensed-phase heat release per unit volume $\dot{q}_c$ is determined by the net effect of the endothermic decomposition (R1) and the exothermic reaction of NO_2 and aldehydes (R2). The in-depth boundary conditions associated with Eqs. (18) and (19) are $T = T_i$ and $Y_p = 1$, respectively, where T_i is the initial (conditioned) temperature of the propellant. The surface conditions require that the propellant decomposition be completed (i.e., $Y_p = 0$) and $T = T_s$.

C. Interfacial Boundary Conditions

The processes in the gas and condensed phases are matched at the propellant surface by requiring continuities of mass and energy. This procedure eventually determines the propellant burning rate and surface conditions of temperature and species concentrations.

With the application of conservation laws to the gas-solid interface, the matching conditions are expressed as follows:

Mass balance for the mixture

$$(\rho v)_g = -\rho_c r_b \tag{20}$$

Mass balance for species i

$$[\rho(v + \hat{v}_i)Y_i]_g = -\rho_c r_b Y_{i,s} \tag{21}$$

Energy balance

$$-\lambda_g \left(\frac{\partial T}{\partial y}\right)_g + \left[\rho \sum_{i=1}^{N} Y_i h_i (v + \hat{v}_i)\right]_g = -\lambda_c \left(\frac{\partial T}{\partial y}\right)_s - \rho_c r_b \left[C_c(T_s - T_{\text{ref}}) + \sum_{i=1}^{N} Y_i h_{f,i}^0\right]_s \tag{22}$$

Subscripts g and s represent conditions at the interface on the gas and solid sides, respectively. Under steady-state conditions, the net heat flux to the condensed phase can be obtained by integrating the energy equation for the condensed phase, yielding

$$\lambda_c \left(\frac{dT}{dy}\right)_s = \rho_c r_b [C_c(T_s - T_i) - Q_c] \tag{23}$$

where Q_c is the total heat release in the condensed phase. Equations (20–22), along with the condition that $Y_p = 0$ at the interface, are sufficient to solve the set of unknowns (v, r_b, T, Y_i) at the propellant surface.

In addition to the above boundary conditions, the no-slip condition ($u = 0$) is imposed at the gas-solid interface. Pressure is deduced from the momentum balance normal to the propellant surface.

III. Numerical Method

The theoretical formulation summarized in the preceding section presents a stringent challenge for computational efficiency. There are several well-recognized reasons for this difficulty, including slow convergence and large round-off error at low Mach numbers, numerical stiffness associated with chemical reactions, and entangled coupling of physicochemical processes between gas and condensed phases. A brief summary of various computational problems encountered in an analysis of rocket-motor internal flow is given in Ref. 5.

In view of the deficiencies in existing numerical schemes for treating propellant combustion in rocket motors, the authors have developed an implicit dual time-stopping integration method,[5,16,17] which has proven to be quite efficient and robust for reacting flows at all speeds. The algorithm first employs pressure decomposition and preconditioning techniques to circumvent difficulties for low-speed compressible flows, a basic requirement for treating acoustic oscillations in a rocket motor. A fully coupled implicit formulation is then used to enhance numerical stability and efficiency. The scheme has the advantage of achieving a high degree of temporal accuracy with only a modest increase in computational cost. Moreover, since the governing equations are solved implicitly, the numerical method is very stable, and allows the selection of the integration time step to be dictated by physical processes rather than numerical stability.

IV. Strand Burning Characteristics

The chemical kinetics scheme is first validated against measurements of strand-burning characteristics over a pressure range of 1–100 atm. The analysis is based on one-dimensional treatment of the conservation equations in both the gas and condensed phases, along with the set of reaction mechanisms, (R1–R7), for the chemical pathways. Major ingredients of the propellant are 52% NC and 43% NG, simulating one of the propellants (code number EC-1) investigated in Ref. 15. Thermochemical parameters used in the present study are compiled from Refs. 11 and 13, as listed in Table 1. The heat of combustion for reaction (R6), Q_{NO}, is adjusted to match

Table 1 Thermochemical parameters of double-base propellant

Parameter	Value	Reference
E_c	167.4, kJ/mole	13
E_{NO_2}	20.9, kJ/mole	13
E_{CH_2O}	104.7, kJ/mole	12
$E_{(CHO)_2}$	83.7, kJ/mole	12
E_{NO}	209.3, kJ/mole	11
E_{carb}	129.8, kJ/mole	8
B_c	1.0×10^{17}, 1/s	13
B_{NO_2}	1.3×10^{6}, 1/s	—
A_{NO_2}	1.0×10^{5}, 1/s	11
A_{CH_2O}	5.0×10^{8}, m^3/kg.s	12
$A_{(CHO)_2}$	5.0×10^{8}, m^3/kg.s	12
A_{NO}	5.0×10^{8}, m^3/kg.s	11
A_{carb}	2.8×10^{7}, 1/s	11
Q_c	−135, kcal/kg	13
Q_{NO_2}	1040, kcal/kg	13
Q_{CH_2O}	389, kcal/kg	13
$Q_{(CHO)_2}$	−539, kcal/kg	13
Q_{NO}	1900, kcal/kg	—
Q_{carb}	1600, kcal/kg	10
ρ_c	1620, kg/m^3	13
C_p	0.35, kcal/kg.K	11
C_c	0.40, kcal/kg.K	11
λ_g	2.5×10^{5}, kcal/m.s.K	11
λ_c	7.0×10^{5}, kcal/m.s.K	11

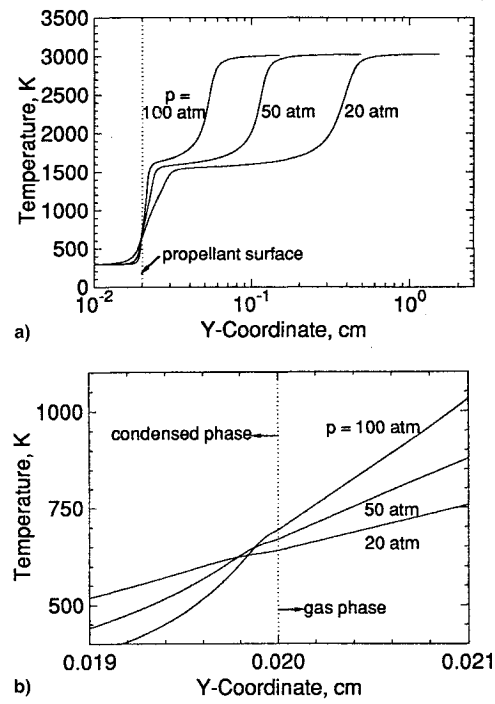

Fig. 2 Temperature distributions in condensed and gas phases at various pressures: a) entire combustion wave and b) close-up view near surface.

Table 2 Species concentrations of double-base propellant combustion

	NO_2	CH_2O	$(CHO)_2$	NO	N_2	CO	CO_2	H_2O	H_2	(HC)	C
					At burning surface						
9 atm, Ref. 9	0.330	0.18	0.168	0.085	0.0	0.10	0.07	0.027	0.0	0.0	0.04
11 atm, Ref. 12	0.255	0.21	0.100	0.140	0.0	0.09	0.10	0.060	0.0	0.0	0.05
10 atm, current	0.274	0.22	0.108	0.136	0.0	0.09	0.10	0.040	0.0	0.0	0.03
					End of primary flame						
9 atm, Ref. 9	0.0	0.0	0.0	0.247	0.021	0.41	0.147	0.139	0.006	0.026	0.0
11 atm, Ref. 12	0.0	0.0	0.0	0.260	0.040	0.34	0.180	0.140	0.007	0.040	0.0
10 atm, current	0.0	0.0	0.0	0.250	0.030	0.33	0.210	0.135	0.006	0.030	0.0
					End of secondary flame						
9 atm, Ref. 9	0.0	0.0	0.0	0.0	0.150	0.280	0.380	0.190	0.004	0.0	0.0
10 atm, Ref. 16	0.0	0.0	0.0	0.0	0.149	0.288	0.348	0.185	0.004	0.0	0.0
10 atm, current	0.0	0.0	0.0	0.0	0.147	0.286	0.378	0.185	0.004	0.0	0.0

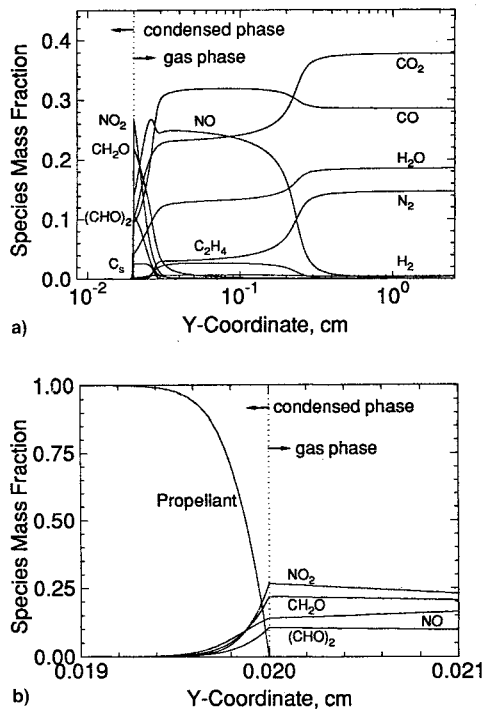

Fig. 3 Distributions of species concentrations in condensed and gas phases at 20 atm: a) entire combustion wave and b) close-up view near surface.

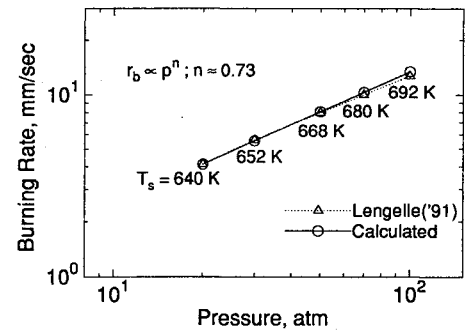

Fig. 4 Effect of pressure on propellant burning rate and surface temperature.

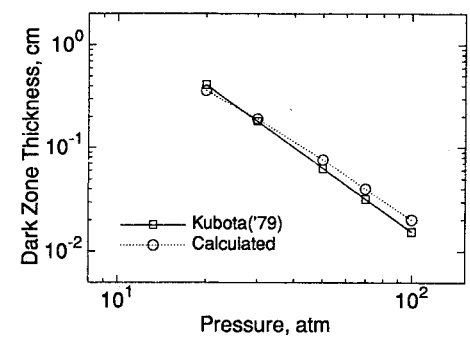

Fig. 5 Effect of pressure on dark-zone thickness.

the final flame temperature predicted by the NASA chemical equilibrium analysis.[18]

Figure 2 shows the distributions of temperature at three different pressures. The flame structure is characterized by three distinct regimes corresponding to primary flame (fizz), dark, and secondary (final luminous) flame zones. The temperature increases rapidly from the surface to around 1600 K in the dark zone, and finally levels off in the secondary flame. A close-up view of the temperature field near the surface is also presented. The slowdown in temperature increase immediately underneath the surface is attributed to the heat release in the thin superficial degradation layer where the thickness is less than 10 μm. Figure 3 presents the species-concentration profiles in the entire flame zone and a close-up view near the surface. The overall reaction mechanisms can be globally grouped into the following steps: 1) molecular degradation and ensuing exothermic reactions of NO_2 and aldehydes in the subsurface layer; 2) generation of NO, CO, CO_2, and H_2O, as well as removal of NO_2 and aldehydes in the primary flame; and 3) reduction of NO to form the final products such as N_2, CO_2, H_2, etc., in the secondary flame. A two-stage chemical pathway in the gas phase is clearly observed. Table 2 presents the comparison with experimental data measured at various locations by means of gas chromatography and mass spectrometry techniques. Good comparison between predictions and measurements is achieved.

The effects of pressure on burning rate and surface temperature are also studied, giving the result shown in Fig. 4. The pressure exponent in the Saint-Robert type of burning-rate law ($r_b \sim p^n$) is 0.73, consistent with experimental observations.[12] The surface temperature increases from 640 K at 20 atm to 692 K at 100 atm, owing to enhanced exothermic reactions at high pressures and their influence on heat transfer to the propellant surface. It is worth noting that the subsurface degradation reaction is not affected directly by pressure, but rather by the near-field heat release process in which pressure plays an important role. Figure 5 shows the pressure dependence of dark-zone thickness, which is defined as the distance between the two inflection points in the temperature profile.

The dark zone thickness decreases exponentially with increasing pressure. The highly exothermic NO reduction at elevated pressure tends to merge the secondary flame with the primary flame, and consequently, causes the temperature plateau in the dark zone to vanish.

V. Interactions between Acoustic Oscillations and Flame Dynamics

After validation of the chemical kinetics model, the analysis summarized in Sec. II is implemented to study motor internal flows coupled with propellant combustion at 60 atm. The chamber, which is closed upstream, measures 0.6 m in length and 5.08 cm in height. Only the upper half of the volume is treated because of the symmetry of flow properties with respect to the centerline. The mass flux entering the chamber from the propellant surface is about 14.21 kg/m^2 s, based on the strand burning rate. The corresponding injection Mach number determined by the local flow condition is 9×10^{-4}. Although the maximum Reynolds number at the exit is 10^5 and turbulence may occur in the downstream portion of the chamber, the flow remains basically laminar near the surface due to propellant burning.[5] Thus, the present study considers only laminar flow, with emphasis placed on the interactions between acoustic oscillations and flame dynamics in the gas phase. The effect of turbulence on local flow structure has been addressed in detail in Ref. 5 for situations under steady operations, and will be further examined elsewhere for cases involving acoustic waves. The computational grid for the gas phase consists of 80 and 90 points in the axial and vertical directions, respectively, while the condensed-phase grid is composed of 80 and 25 points in the corresponding directions. The grids are clustered near the burning surface to resolve the steep gradients of temperature and species concentrations in the near field. The computational domain for the condensed phase is 100 μm, with the smallest grid spacing normal to the surface about 1.7 and 0.1 μm, respectively, in the gas and condensed phases.

The steady-state flowfield must be obtained first to provide the initial conditions for analysis of unsteady motions. A comprehensive study of steady motor internal flow and combustion-wave structure (including the effects of pressure and crossflow on propellant burning characteristics) by the authors is presented in Ref. 5. With this steady-state solution as a known condition, periodic pressure oscillations are imposed at the chamber exit to simulate acoustic oscillations of the longitudinal standing wave in the motor. The propellant mass burning rate is fixed at its steady-state value, thereby enabling a systematic investigation into the unsteady heat-release mechanism in the gas phase without complications resulting from the coupling with the condensed-phase processes. The transient combustion response of propellant to ambient flow disturbances and its ensuing influence on acoustic waves is addressed in companion work.[4] The amplitude of the pressure oscillation is 2% of the mean pressure; the frequencies are 877.5 and 1755.1 Hz, corresponding to the first and second modes, respectively. Data analysis of flow characteristics is conducted after steady oscillations are achieved in the sixth cycle of the imposed acoustic oscillations.

A. Pressure and Velocity Fields

Figure 6, which shows the instantaneous distributions of acoustic pressure at four different times within one cycle of oscillation for the first and second modes, exhibits well-defined standing waves in the chamber. The corresponding contour plots for the first mode are given in Fig. 7. The low Mach-number environment basically renders a one-dimensional pressure field, with no discernible variation in the vertical direction. The phenomenon of acoustic refraction, commonly observed for waves traveling in a nonuniform medium, is not evident here. Figures 8 and 9 show the evolution of the

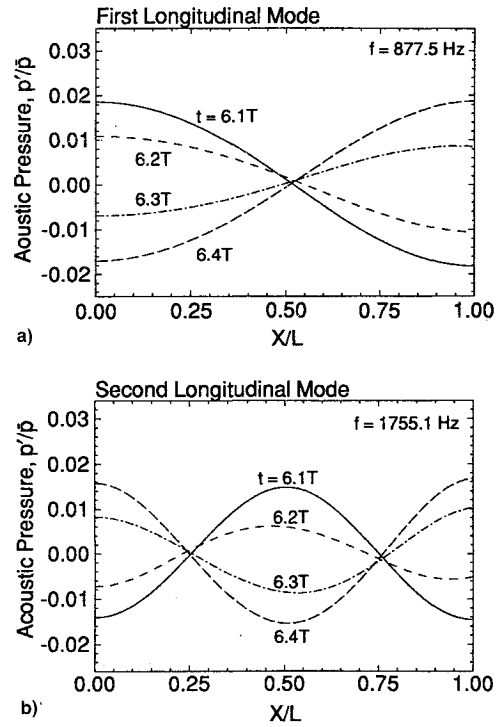

Fig. 6 Time evolution of acoustic pressure field: a) first and b) second longitudinal mode.

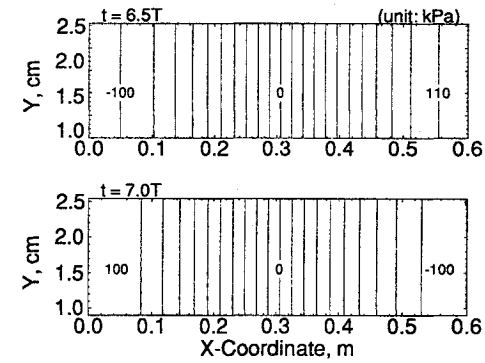

Fig. 7 Contour plots of acoustic pressure; first mode.

axial velocity fields of the first and second modes, respectively. Only the upper portion of the chamber is presented in order to obtain better spatial resolution of the flowfield. The complex structure adjacent to the surface indicates the presence of an acoustic boundary layer within which rapid velocity fluctuations arising from unsteady shear wave[19,20] and flame oscillations[21,22] occur. The physicochemical processes involved are extremely intricate, including interactions among all three modes of acoustic, vortical, and entropy disturbances. The axial acoustic oscillation may couple with the mass flow entering the chamber from the surface and generate fluctuating vorticity to satisfy the no-slip boundary condition. The same acoustic wave can also affect the heat-release mechanism in the flame zone and produce entropy fluctuations based on the local flame dynamics. Both ensuing vorticity and entropy disturbances are then smoothed out by viscous dissipation and heat condition during their convection downstream by the mean flow. Consequently, a simple acoustic field is rendered in the core-flow region, with a one-dimensional distribution of velocity fluctuation, which is consistent with classic acoustic theory. The general subject of mutual coupling among acoustic, vortical, and entropy modes is discussed comprehensively within the context of solid rocket

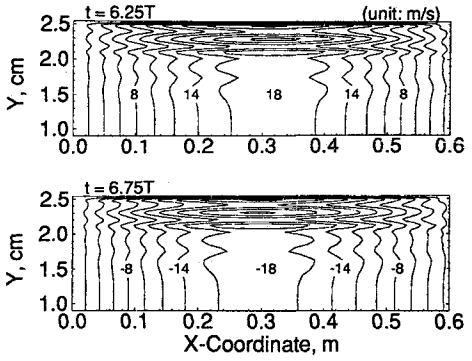

Fig. 8 Contour plots of axial velocity fluctuation; first mode.

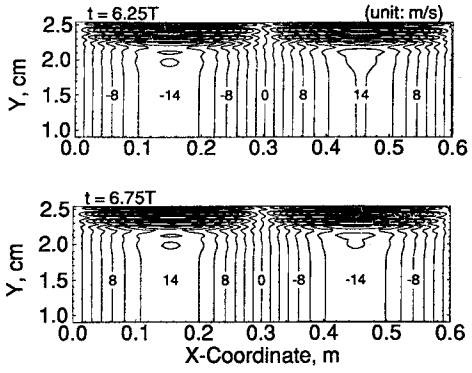

Fig. 9 Contour plots of axial velocity fluctuation; second mode.

combustion instability by the authors in Refs. 21 and 22. The acoustic boundary-layer thickness, defined by the vertical location at which the shear-wave amplitude decays to less than 1% of the acoustic-velocity amplitude, of the first mode is about twice that of the second mode. For nonreacting motor flows treated in Refs. 19 and 20, this thickness was found to depend on two Reynolds numbers: one related to the gas particle velocity at the surface, and the other to the acoustic particle velocity or frequency. Since the gas surface velocity is fixed in the present study, the frequency appears to be the only major reason for the difference in the observed acoustic boundary-layer thickness.

The nonuniformity of the velocity field can be further examined in Figs. 10 and 11, which show the vertical distributions of the axial velocity fluctuation u' for the first and second modes, respectively. Both amplitudes and phases are presented to achieve a better understanding of this complicated structure. Also included is the flame thickness defined by the location at which the temperature reaches 97% of the final flame temperature. The axial velocity fluctuation u' increases rapidly in the near field due to unsteady vorticity generation, then oscillates spatially with a decaying amplitude as the shear wave propagates into the core flow, and finally reaches one-dimensional distribution in the bulk of the chamber. Compared with the cold-flow simulation in which chemical reactions are not involved,[19,20] the first peak in u' near the surface is much smaller than the second peak. This phenomenon may be caused by the rapid increase of temperature in the flame zone. The strong variation of acoustic impedance, approximately proportional to the inverse of $\sqrt{T}$, significantly modifies the distribution of u' although the acoustic pressure remains nearly one-dimensional. u' usually attains its maximum amplitude beyond the major heat-release region. The flame tends to suppress the shear flow disturbance.[21,22] In the core-flow region where the shear wave vanishes, the behavior of u' follows the isentropic relation with the acoustic pressure, with a phase lag of 90 deg with reference to p'.

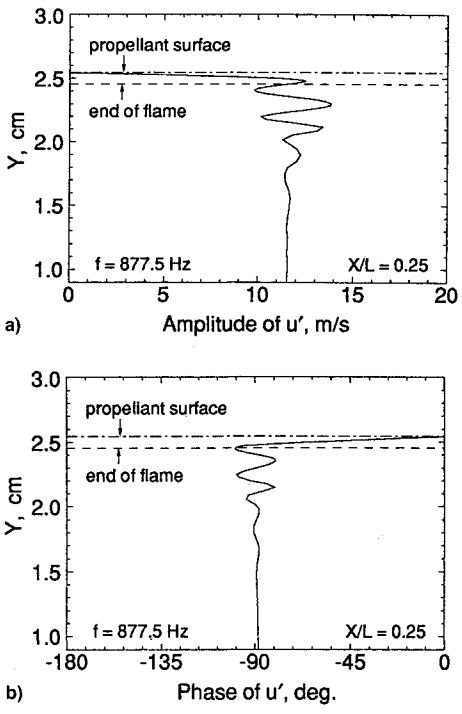

Fig. 10 Vertical distributions of axial velocity fluctuation of first mode at $x/L = 0.25$: a) amplitude and b) phase.

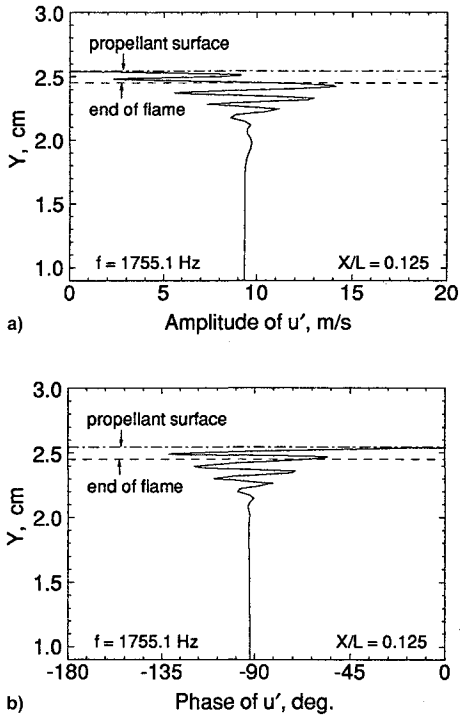

Fig. 11 Vertical distributions of axial velocity fluctuation of second mode at $x/L = 0.125$: a) amplitude and b) phase.

Figure 12 shows the distributions of the amplitude and phase of the vertical velocity fluctuation v' at various axial locations for the first mode. A logarithmic scale is adopted for the vertical coordinate to clearly indicate the variations near the burning surface. In the present study in which the propellant mass burning rate is fixed at its steady-state value, v' varies slightly near the surface due to density fluctuation associated with the acoustic pressure oscillation. However, a substantial increase in the amplitude of v' is observed in the secondary flame zone ($1 - Y/H \approx 0.02$) as a result of the huge density

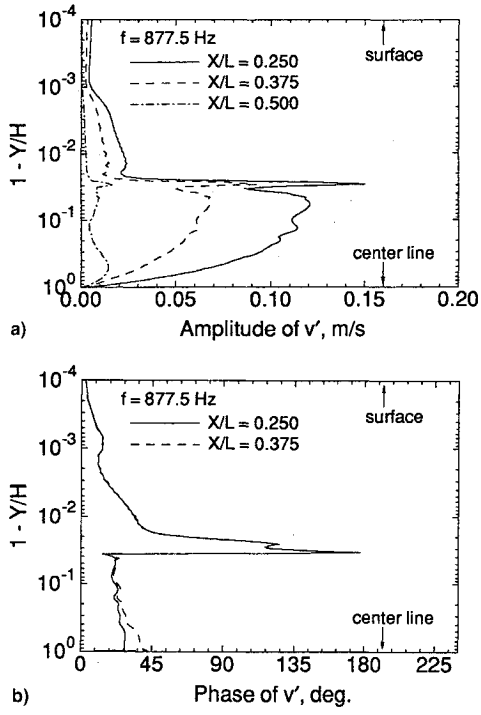

Fig. 12 Distributions of vertical velocity fluctuation of first mode at various axial locations: a) amplitude and b) phase.

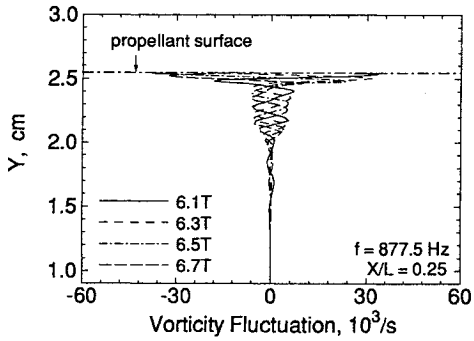

Fig. 13 Instantaneous distributions of vorticity fluctuation of first mode at $x/L = 0.25$.

change across the flame. Any small perturbation of the flame location may lead to an appreciable change in v'. This phenomenon is further evidenced by the steep distribution of the phase in the secondary flame. It should be mentioned that v' reaches its minimum at the acoustic pressure nodal point ($x/L = 0.5$), but not at the acoustic velocity nodal point. The interaction between unsteady motions and flame dynamics is basically a pressure-coupled phenomenon, at least in the present study, which does not include the effect of turbulence.

The result of the unsteady vortical field study is shown in Fig. 13 for the first mode. In a two-dimensional flow without heat release or viscous effect, the vorticity of a given fluid particle is conserved. However, the conservation property of vorticity is no longer valid for a viscous reacting flow due to viscous dissipation, volume dilatation, and baroclinicity resulting from misalignment between the density and pressure gradients.[21-23] In general, viscous dissipation has a negligible effect on vorticity transport in the flame zone where density varies so dramatically that volume dilatation and baroclinicity become predominant. The rate of vorticity change slows down rapidly beyond the flame zone, and decays gradually toward the core-flow region. This agrees with the observation that the flame expands the distribution of vorticity when the vortex passes through the premixed flame.[24]

B. Temperature Field and Heat-Release Mechanisms

Figures 14 and 15 show the vertical distributions of temperature fluctuation at various times for the first and second modes, respectively. The steady-state temperature profiles denoted by the dashed lines are also presented to facilitate discussion. The most significant phenomenon observed for both modes of oscillation is the occurrence of a large temperature oscillation in the luminous flame zone where the major reaction is the reduction of NO species. The maximum amplitude of temperature fluctuation in the core-flow region

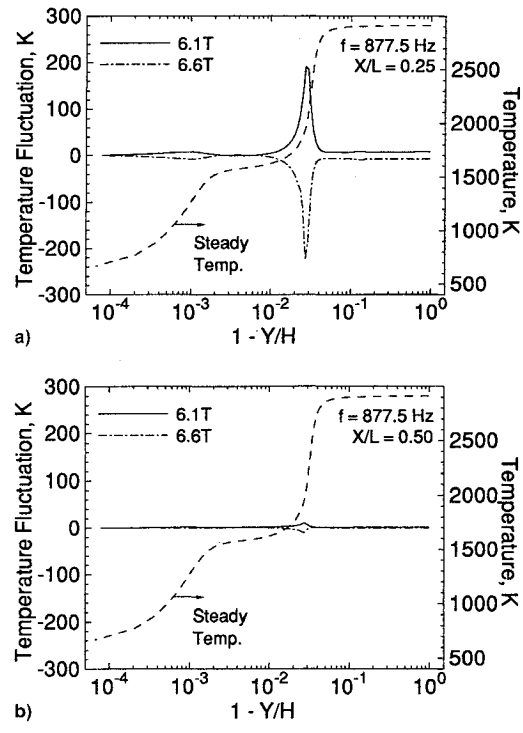

Fig. 14 Instantaneous distributions of temperature fluctuation of first mode. x/L = a) 0.25 and b) 0.5.

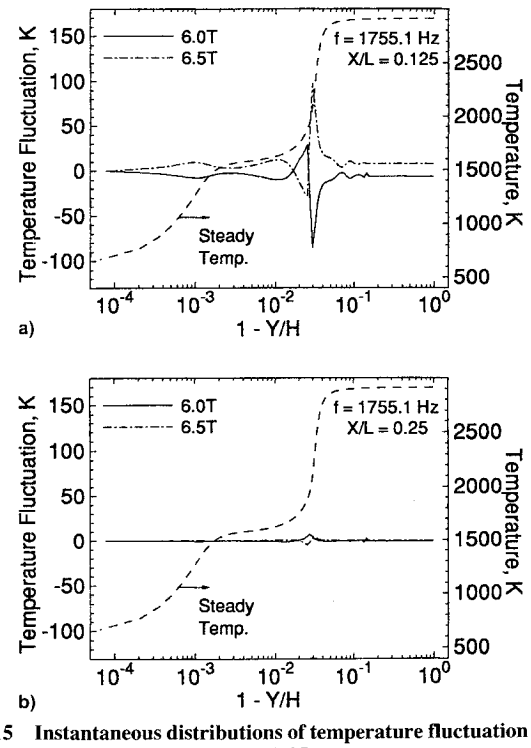

Fig. 15 Instantaneous distributions of temperature fluctuation of second mode. x/L = a) 0.125 and b) 0.25.

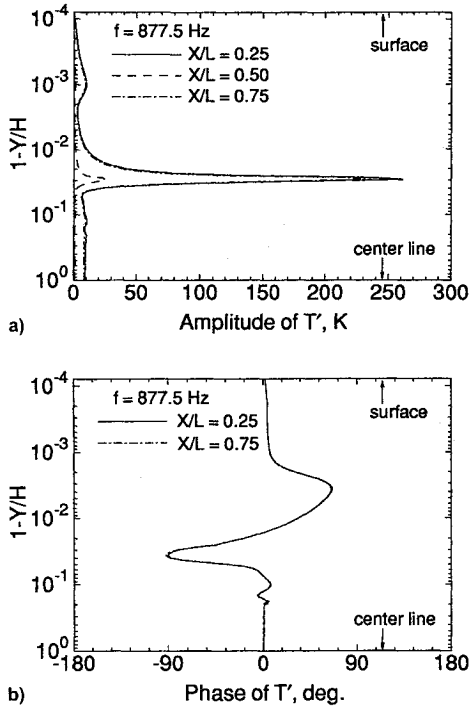

Fig. 16 Vertical distributions of temperature fluctuation of first mode at various axial locations: a) amplitude and b) phase.

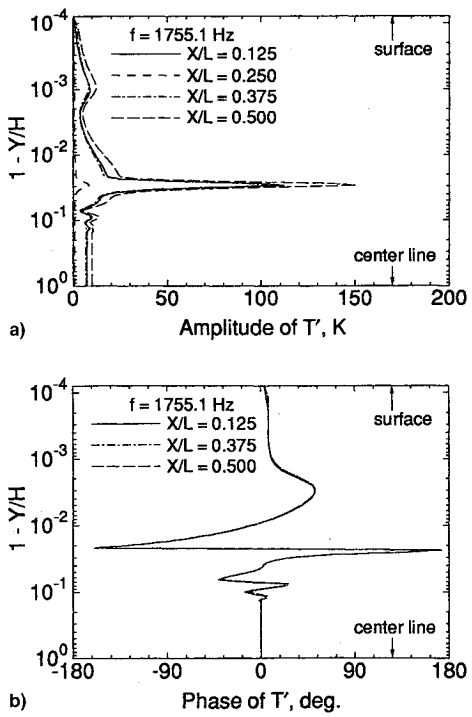

Fig. 17 Vertical distributions of temperature fluctuation of second mode at various axial locations: a) amplitude and b) phase.

is about 10 K, corresponding to the isentropic variation with the acoustic pressure, since this region has no chemical reaction and negligibly small viscous stress. Figures 16 and 17 show the vertical distributions of the amplitude and phase of temperature fluctuation for the first and second modes, respectively. Strong coupling between flame dynamics and acoustic waves is observed in the flame zone, except in regions near the pressure nodal points where the acoustic pressure reaches its minimum value. The flame moves periodically in the vertical direction in response to local pressure oscillations,

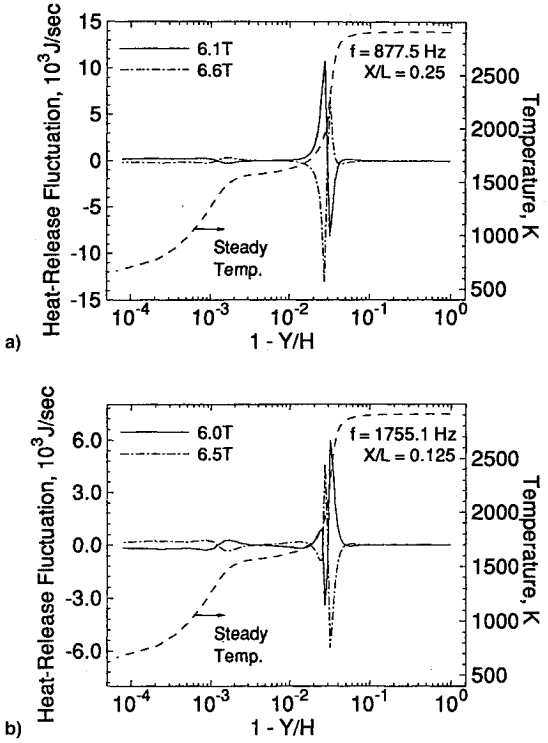

Fig. 18 Instantaneous distributions of heat-release fluctuation: a) first and b) second mode.

thereby rendering an almost symmetric distribution of temperature fluctuation across the luminous flame front for the first acoustic mode (see Fig. 14). However, the nonsteady temperature profile reveals a slightly asymmetric shape for the second mode, with positive and negative peaks observed. This can be explained by considering the influence of the shear wave on the near-field flame structure. For the first longitudinal mode, the shear wave reaches its peak value in the flame zone and completes the first cycle above the flame. For the second mode, the shear wave finishes its first cycle completely in the flame zone with the second peak occurring still inside the flame. The local interactions between the shear wave and flame dynamics dictate the spatial distribution and temporal evolution of the temperature fluctuation.

Figure 18 shows the time evolution of the heat-release fluctuation for both modes. The behavior of the heat-release fluctuation closely follows the gradient of the temperature fluctuation, easily explained by the energy balance over a gas-phase control volume. Since the heat-release rate is simply proportional to the spatial gradient of temperature, the effects of both thermal inertia and diffusion are shown to be small compared with the convection process. The flame behaves quasisteadily in response to imposed pressure oscillation.

C. Rayleigh's Criterion

The effect of heat release on motor stability characteristics can be investigated using Rayleigh's criterion,[25] which determines the conditions for driving or suppressing flow oscillations when thermal energy is added periodically to acoustic fields. The mathematical formulation for this criterion is written as

$$\int_V \int_\tau p'(\boldsymbol{r}, t) q'(\boldsymbol{r}, t)\, \mathrm{d}t\, \mathrm{d}v \tag{24}$$

An acoustic wave can be excited if the previous integral is a positive value, and damped if negative. The results using Rayleigh's criterion for the first and second modes of oscillation are presented in Fig. 19. The quantity $\langle p'q' \rangle$, referred

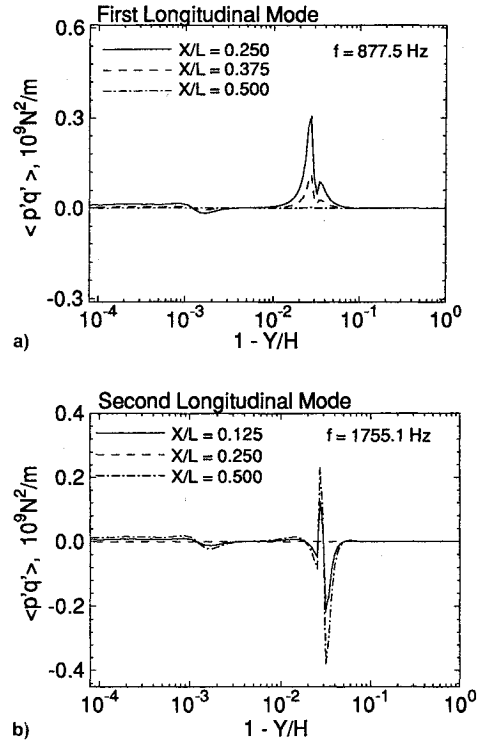

Fig. 19 Vertical distributions of Rayleigh's parameter at various axial locations: a) first and b) second mode.

to as Rayleigh's parameter, is obtained by time-averaging the product of acoustic pressure and heat-release fluctuations over one cycle of oscillation. The nonsteady heat release in the flame zone exhibits a complicated mechanism for driving and suppressing acoustic oscillations, as evidenced by the positive and negative values of $\langle p'q' \rangle$. The fizz zone (primary flame) has little influence in the determination of the motor stability characteristics. However, the dynamic response of heat release in the luminous flame zone plays a decisive role, with large excursions of temperature and heat-release fluctuations occurring in that region. For both the first and second modes of oscillation, the net value of $\langle p'q' \rangle$ over the entire chamber is positive. The nonsteady heat release arising from the interactions between acoustic waves and flame dynamics tends to drive flow oscillations in the motor, and can be treated as a combination of monopole and dipole sources.

VI. Conclusions

A comprehensive numerical analysis has been developed to study the interactions between acoustic waves and gas-phase flame dynamics of a double-base homogeneous propellant in a rocket motor. The formulation treats the complete conservation equations of mass, momentum, energy, and species concentration, and accounts for finite rate chemical kinetics in the gas phase and subsurface reactions. The governing equations and associated boundary conditions are solved numerically using a fully coupled implicit scheme based on a dual time-stepping integration algorithm.

In order to simulate the flame structure of the solid propellant, a chemical kinetics model is first established. The model adopts two reactions for the condensed phase and five reactions for the gas phase. The results from one-dimensional, steady, and isobaric flow calculations are consistent with experimental data for burning rates, temperature distributions, dark-zone thicknesses, and species concentrations. The chemical kinetics model is proven to be suitable for present study of double-base propellant combustion.

The model has been implemented to examine the detailed flow structures and heat-release mechanisms in various parts of the motor, including microscale motions near the propellant surface and macroscale motions in the bulk of the chamber. Results indicate that strong interactions between exothermic reactions and acoustic waves occur in regions with steep temperature gradients due to the large activation energy of the associated chemical kinetics. The dynamic behavior of the luminous flame plays a decisive role in determining the motor stability characteristics. The distributed combustion response in the gas phase provides the energy for driving flow oscillations, and, based on acoustic theory, can be treated correctly as a combination of monopole and dipole sources. The classical treatment of motor stability by means of combustion response or acoustic admittance functions appears too simplistic, and requires substantial revision to accommodate the actual physicochemical processes involved.

Acknowledgments

This work was sponsored by the Air Force Office of Scientific Research under Grant F49620-93-1-0430. The support and encouragement of Mitat A. Birkan is greatly appreciated.

References

[1]Culick, F. E. C., "A Review of Calculations for Unsteady Burning of a Solid Propellant," *AIAA Journal*, Vol. 6, No. 12, 1968, pp. 2241–2255.

[2]Novozhilov, B. V., "Theory of Nonsteady Burning and Combustion Stability of Solid Propellants by the Zeldovich-Novozhilov Method," *Nonsteady Burning and Combustion Stability of Solid Propellants*, edited by L. De Luca, E. W. Price, and M. Summerfield, Vol. 143, Progress in Astronautics and Aeronautics, AIAA, Washington, DC, 1992, pp. 601–641.

[3]Culick, F. E. C., and Yang, V., "Prediction of the Stability of Unsteady Motions in Solid Propellant Rocket Motors," *Nonsteady Burning and Combustion Stability of Solid Propellants*, edited by L. De Luca, E. W. Price, and M. Summerfield, Vol. 143, Progress in Astronautics and Aeronautics, AIAA, Washington, DC, 1992, pp. 719–779.

[4]Roh, T. S., and Yang, V., "Transient Combustion Response of Solid Propellants to Acoustic Disturbances in Rocket Motors," AIAA Paper 95-0402, 1995; also *Journal of Propulsion and Power* (submitted for publication).

[5]Tseng, I. S., and Yang, V., "Combustion of a Double-Base Homogeneous Propellant in a Rocket Motor," *Combustion and Flame*, Vol. 96, 1994, pp. 325–342.

[6]McBride, B. J., Gordon, S., and Reno, M. A., "Coefficients for Calculating Thermodynamic and Transport Properties of Individual Species," NASA TM-4513, 1993.

[7]Reid, R. C., Prausnitz, J. M., and Poling, B. E., *The Properties of Gases and Liquids*, 4th ed., McGraw–Hill, New York, 1987, pp. 407–410.

[8]Song, Y. H., Beer, J. M., and Sarofim, A. F., "Reduction of Nitric Oxide by Coal Char at Temperatures of 1250–1750K," *Combustion Science and Technology*, Vol. 25, 1981, pp. 237–240.

[9]Cohen, N. S., "Combustion Chemistry of Nitrate Ester-Based Propellants," AIAA Paper 83-1198, 1983.

[10]Lengelle, G., Bizot, A., Duterque, J., and Trubert, J. F., "Steady-State Burning of Homogeneous Propellants," *Fundamentals of Solid-Propellant Combustion*, edited by K. K. Kuo and M. Summerfield, Vol. 90, Progress in Astronautics and Aeronautics, AIAA, New York, 1984, pp. 361–407.

[11]Bizot, A., and Beckstead, M. W., "A Model for Double-Base Propellant Combustion," *Proceedings of the 22nd Symposium (International) on Combustion*, The Combustion Inst., Pittsburgh, PA, 1988, pp. 1827–1834.

[12]Faddoul, F., Most, J. M., and Joulain, P., "Combustion Kinetic of a Homogeneous Double Base Propellant," *Dynamics of Deflagrations and Reactive System—Flames*, edited by A. L. Kuhl, Vol. 131, Progress in Astronautics and Aeronautics, AIAA, Washington, DC, 1989, pp. 275–296.

[13]Lengelle, G., Duterque, J., Godon, J. C., and Trubert, J. F., "Solid Propellant Steady Combustion: Physical Aspects," AGARD Lecture Series 180, 1991.

[14]Kubota, N., "Determination of Plateau Burning Effect of Catalyzed Double-Base Propellant," *Proceedings of the 17th Symposium (International) on Combustion*, The Combustion Inst., Pittsburgh, PA, 1979, pp. 1435–1441.

[15]Aoki, I., and Kubota, N., "Combustion Wave Structures of High- and Low-Energy Double-Base Propellants," *AIAA Journal*, Vol. 20, 1982, pp. 100–105.

[16]Withington, J. P., Shuen, J. S., and Yang, V., "A Time-Accurate Implicit Method for Chemically Reacting Flows at All Mach Numbers," AIAA Paper 91-0581, 1991.

[17]Hsieh, S. Y., and Yang, V., "A Preconditioned Flux-Differencing Scheme for Chemically Reacting Flows at All Mach Numbers," *International Journal of Computational Fluid Dynamics* (submitted for publication).

[18]McBride, B. J., Reno, M. A., and Gordon, S., "CET93 and CETPC: An Interim Updated Version of the NASA Lewis Computer Program for Calculating Complex Chemical Equilibria with Applications," NASA TM-4557, 1994.

[19]Flandro, G. A., "Effects of Vorticity Transport on Axial Acoustic Waves in a Solid Propellant Rocket Chamber," American Society of Mechanical Engineers Annual Winter Meeting, Dec. 1989.

[20]Flandro, G. A., "Effects of Vorticity on Rocket Combustion Instability," *Journal of Propulsion and Power*, Vol. 11, No. 4, 1995, pp. 607–625.

[21]Tseng, C. F., Chu, W. W., and Yang, V., "Interactions of Acoustic Waves and Premixed Flames in Porous Chambers, I: Numerical Simulation," *Combustion and Flame* (submitted for publication).

[22]Chu, W. W., Tseng, C. F., and Yang, V., "Interactions of Acoustic Waves and Premixed Flames in Porous Chambers, II: Theoretical Analysis," *Combustion and Flame* (submitted for publication).

[23]Pedlosky, J., *Geophysical Fluid Dynamics*, Springer–Verlag, New York, 1982, pp. 34–38.

[24]Rutland, C. J., and Ferziger, J. H., "Simulations of Flame-Vortex Interactions," *Combustion and Flame*, Vol. 84, 1991, pp. 343–360.

[25]Rayleigh, J. W. S., *Theory of Sound*, Vol. II, Dover, New York, 1954.